Reveal the Alignment of Defects in a Metal-Organic Framework with Tunable Flexibility

Yao Fu
Zhejiang University

Alexander Forse
University of Cambridge

Zhengzhong Kang
Zhejiang University

Matthew Cliffe
University of Nottingham

Weicheng Cao
Zhejiang University

Jinglin Yin
Zhejiang University

Lina Gao
Zhejiang University

Zhenfeng Pang
Zhejiang University   https://orcid.org/0000-0003-1566-5454

Tian He
Zhejiang University

Qinlong Chen
Zhejiang University

Qi Wang
Zhejiang Uniersity   https://orcid.org/0000-0002-2246-1401

Jeffrey Long
University of California, Berkeley   https://orcid.org/0000-0002-5324-1321

Jeffrey Reimer
University of California, Berkeley   https://orcid.org/0000-0002-4191-3725

Xueqian Kong (✉ kxq@zju.edu.cn)
Zhejiang University   https://orcid.org/0000-0002-1901-9073

Article

Keywords:

Posted Date: April 14th, 2022

DOI: https://doi.org/10.21203/rs.3.rs-1173692/v1

Reveal the Alignment of Defects in a Metal-Organic Framework with Tunable Flexibility

Yao Fu[1,2], Alexander C. Forse[2,3,4], Zhengzhong Kang[1], Matthew J. Cliffe[5], Weicheng Cao[1], Jinglin Yin[1], Lina Gao[1], Zhenfeng Pang[1], Tian He[1], Qinlong Chen[1], Qi Wang[1], Jeffrey R. Long[2,4,6], Jeffrey A. Reimer[2]*, Xueqian Kong[1]*

[1]Department of Chemistry, Zhejiang University, Hangzhou 310027, China.

[2]Department of Chemical and Biomolecular Engineering, University of California, Berkeley, California, 94720, United States.

[3]Department of Chemistry, University of Cambridge, Cambridge CB2 1EW, UK.

[4]Department of Chemistry, University of California, Berkeley, California 94720, United States.

[5]School of Chemistry, University of Nottingham, University Park, Nottingham, NG7 2RD, UK.

[6]Materials Sciences Division, Lawrence Berkeley National Laboratory, Berkeley, California 94720, United States.

*Corresponding author. Email: reimer@berkeley.edu; kxq@zju.edu.cn

Abstract: Crystalline materials are often considered to have rigid periodic lattices while soft materials are associated with flexibility and non-periodicity. The continuous evolution of metal-organic frameworks (MOFs) has erased the boundaries between these two distinct conceptions. Flexibility, disorder and defects have been found to be abundant in MOF materials with imperfect crystallinity, and their intricate interplay is poorly understood due to the limited strategies for characterizing disordered structures. Here, we apply advanced nuclear magnetic resonance (NMR) spectroscopy to elucidate the mesoscale structures in a defective MOF with a partially disordered lattice. We show that engineered defects can tune the degree of lattice flexibility by combining both ordered and disordered compartments. The one-dimensional alignment of defects is the key for the reversible topological transition.

Main Text:

Structural flexibility can bring unusual properties such as negative gas adsorption[1], stimuli-responsiveness[2], and stereochemical selectivity[3,4] to porous materials. Metal-organic frameworks (MOFs), as an emerging class of porous materials, are endowed with tunable functionalities and diverse three-dimensional topologies[5,6]. Flexibility in MOFs[7] manifests as localized structural changes, e.g. linker rotation[8], or as correlated structural changes such as volume expansion and subunit displacement[9–11]. In addition, the flexibility in MOFs is often associated with defects and disorder, showing the crossover characteristics of crystalline frameworks and soft materials[12–15]. The integration of crystalline and disordered compartments as well as local and correlated structural dynamics have advanced into the new frontiers of solid-state chemistry[16–18]. However, the merits of defects and disorder in MOFs have long been underappreciated, largely because they are inaccessible by common characterization techniques. Novel techniques and strategies are required to uncover the intricate interplay between flexibility, disorder, and defects in these hybrid solids.

In this work, we engineered a new type of defect and created a tunable degree of flexibility in the framework Mg_2(dobpdc) (dobpdc^{4-} = 4,4′-dioxido-3,3′-biphenyldicarboxylate)[19–21] by introducing non-bridging ligand modulators (fluorinated salicylic acid). This MOF represents a widely utilized structural analog of MOF-74[22,23] that adopts a honeycomb-like topology and features open metal sites. Defects in similar MOFs can lead to enhanced performance for adsorption or catalysis[24–29], yet the critical information of defect structure and arrangement has not been revealed. The amorphization of MOF matrices with defects hampers structure determination by diffraction and microscopy techniques[30–32].

We hypothesized that a combination of advanced solid-state nuclear magnetic resonance (SSNMR) techniques[33–38] would be able to decode the arrangement of defects in partially amorphized Mg_2(dobpdc). Spatially interconnected multi-spin interactions (e.g., ^{13}C-^{19}F and ^{19}F-^{19}F dipolar couplings) can map the location and distribution of defects beyond single unit cells and are sensitive to both local and correlated dynamic changes[33,39,40]. The results of our experiments show that defective Mg_2(dobpdc) frameworks undergo a reversible topological (order-to-disorder) transition upon the removal or re-introduction of solvent. This flexible transition can be easily tuned by varying the stoichiometric ratio of defect-forming modulators. Assisted by molecular dynamics (MD) simulations, we show that the defects are aligned in a one-dimensional fashion along the framework channel axis. Our study demonstrates an illustrative case of a MOF material wherein defects, disorder and flexibility synergize, and the investigation provides new understanding of hybrid structures on the mesoscale.

Results and Discussion

Construction of defective Mg_2(dobpdc)

Defect-containing Mg_2(dobpdc) samples were synthesized by adding varying amounts of 4-fluorosalicylic acid (H_2Fs) to the synthesis mixture (Fig. 1a). Since H_2Fs has only half of the coordination sites (hydroxyl and carboxylate groups) as the H_4dobpdc linker, we hypothesized that Fs^{2-} can partially substitute dobpdc$^{4–}$ linkers in the MOF to create substitutional defects. The defective samples are referred to as "*x*D", where *x* represents the concentration of defects in the MOF. An ideal Mg_2(dobpdc) sample (referred to as "Ideal") was also prepared for comparison. The detailed synthetic procedures are provided in the supporting information. Scanning electron microscope (SEM) images (Fig. 1b) show that with a low concentration of defects (0.03D), the particles form as elongated rods similar to that of the ideal sample. However, for samples with

more defects, the particles grow into large sphere-like or irregular shapes with a distribution of diameters from 3 µm to 15 µm (Fig. S1). Such large particles are clearly polycrystalline aggregates of smaller crystallites.
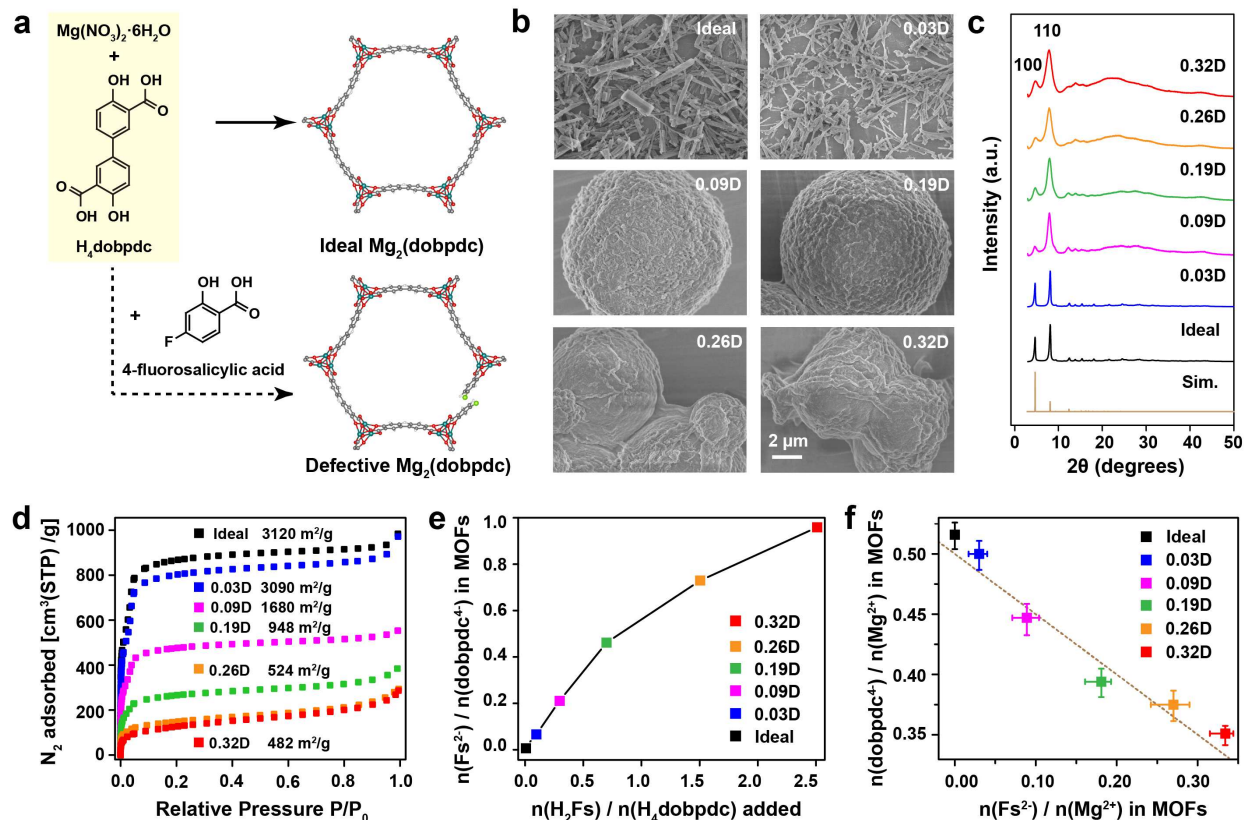

Figure 1. General characterizations of Mg$_2$(dobpdc). (**a**) Schematic illustrations of the preparations for ideal and defective Mg$_2$(dobpdc). (**b**) SEM images of Mg$_2$(dobpdc) samples with various defect concentrations. Scale bar: 2 µm (for all images). (**c**) Powder XRD patterns obtained on as-synthesized Mg$_2$(dobpdc) samples. (**d**) N$_2$ adsorption isotherms measured at 77 K for samples activated under vacuum at 250 °C. The BET surface areas are shown. (**e**) The molar ratios of coordinated Fs^{2-} to dobpdc^{4-} (measured by solution-state ^{1}H NMR of digested samples) plotted against the molar ratios of added H$_2$Fs to H$_4$dobpdc during synthesis. (**f**) The molar ratios of dobpdc^{4-} to Mg^{2+} ($n(\text{dobpdc}^{4-})/n(\text{Mg}^{2+})$) plotted against the molar ratios of Fs^{2-} to Mg^{2+} ($n(\text{Fs}^{2-})/n(\text{Mg}^{2+})$) in the MOF samples. The dotted line indicates the charge balance.

Figure 1c presents the powder X-ray diffraction (PXRD) patterns of as-synthesized MOF samples (with methanol solvent remaining in the pores). As the samples become more defective, the peaks broaden significantly, yet the lattice dimensions are maintained even with a high density of defects. Fitting of the PXRD patterns shows that the lattice parameter a expands by ~1% for as-synthesized defective MOFs (Fig. S2). Assuming the primary contribution to the peak broadening is a finite crystallite size, this corresponds to a decrease in crystallite size from 65 nm (0.03D) to 6 nm (0.32D) upon increasing defect concentration (Fig. S2). The apparent reduction of the {100} diffraction peak in most defective samples can be attributed to the packing disorder of Fs^{2-} ligands (Fig. S3).

The specific Brunauer-Emmett-Teller (BET) surface area of each material was determined from N$_2$ adsorption data collected at 77 K on samples activated at 250 °C (with methanol removed). The

BET surface area of defective $Mg_2(dobpdc)$ decreases from above 3000 m^2/g (as high as that of the ideal sample [41] to ~500 m^2/g as the defect concentration increases (Fig. 1d). Thermogravimetric analysis shows that the series of defective $Mg_2(dobpdc)$ can withstand up to 400 °C in nitrogen flow without significant degradation, suggesting that they are as thermally stable as the ideal sample (Fig. S4).

The chemical composition of each defective $Mg_2(dobpdc)$ sample was studied by solution-state ^{1}H NMR spectroscopy (Fig. S5 and Table S2) and inductively coupled plasma optical emission spectrometry (ICP-OES) (Table S3) on the acid-digested samples. The results (Fig. 1e) show that, by increasing the relative concentration of H_2Fs during synthesis, the quantity of incorporated Fs^{2-} can reach almost a one-to-one ratio with respect to the $dobpdc^{4-}$ linker (as in 0.32D). To understand the stoichiometry in defective $Mg_2(dobpdc)$, we plot the molar ratios of $(dobpdc)^{4-}$ to Mg^{2+} (i.e., $n(dobpdc^{4-})/n(Mg^{2+})$) against the molar ratios of Fs^{2-} to Mg^{2+} (i.e., $n(Fs^{2-})/n(Mg^{2+})$) (Fig. 1f). The analysis shows that the charge balance in defective $Mg_2(dobpdc)$ compounds is maintained: $(+2) \times n(Mg^{2+}) + (-4) \times n(dobpdc^{4-}) + (-2) \times n(Fs^{2-}) = 0$ (marked as the dotted line in Fig. 1f). Therefore, the overall formula for defective $Mg_2(dobpdc)$ can be written as $Mg_2(dobpdc)_{1-x}(Fs)_{2x}$ where x represents the concentration of defects. The removal of x $dobpdc^{4-}$ linkers is compensated by 2x Fs^{2-} modulators, which supports a charge of 2– for the incorporated Fs^{2-} species instead of a protonated form. These findings also support the hypothesis that Fs^{2-} molecules serve as substitutional defects in defective $Mg_2(dobpdc)$ materials.

Reversible order-to-disorder transition

The structural flexibility of defective $Mg_2(dobpdc)$ can be observed on multiple scales using various techniques. The SEM morphology and spectroscopic features of defective $Mg_2(dobpdc)$ (taking 0.32D as an example) undergo dramatic changes when the sample is with or without solvent (methanol). As illustrated in Fig. 2a, the as-synthesized sample, which holds residual methanol in its pores, is referred to here as "wet", the sample dried at room temperature under vacuum, in which the weakly adsorbed methanol was eliminated, is referred to as "dry", and the dried sample re-soaked with methanol (overnight) is referred to as "rewet". Note that the conditions for preparing the "dry" sample are relatively mild (vacuum at room temperature), which should remove weakly adsorbed methanol, yet methanol coordinated to the open metal sites should remain. When weakly adsorbed methanol was removed from the pores, the relatively large aggregated particles (~5 μm) in the "wet" sample turned into smaller blocks (~500 nm) in the "dry" sample. Interestingly, however, the small blocks re-assembled into large particles when the "dry" sample was re-soaked with methanol (Fig. 2b).

In terms of the PXRD patterns (Fig. 2c, S2, S6), the most striking difference between "wet" and "dry" samples is the decrease in intensity of the first Bragg peak ({100}). The loss of intensity of this peak suggests that the long-range ordering of the honeycomb-like structure of $Mg_2(dobpdc)$ has been disrupted in these frameworks. The persistence of a strong {110} peak, which corresponds to the nearest linker-linker distance, suggests that the Mg^{2+} ions remain connected by $dobpdc^{4-}$ linkers in the "dry" samples. The large widths of the peaks make precise determination of lattice parameters via a Pawley refinement of the PXRD patterns challenging, particularly for the *c* parameter (Fig. S2b). However, the *a* parameter contracts by ~1% upon drying the defective samples, as might be expected for the loss of the honeycomb ordering (Fig. S2a). Once the "dry" sample is resoaked in methanol, the long-range ordering is restored as the {100} peak reappears (Fig. 2c and S6).

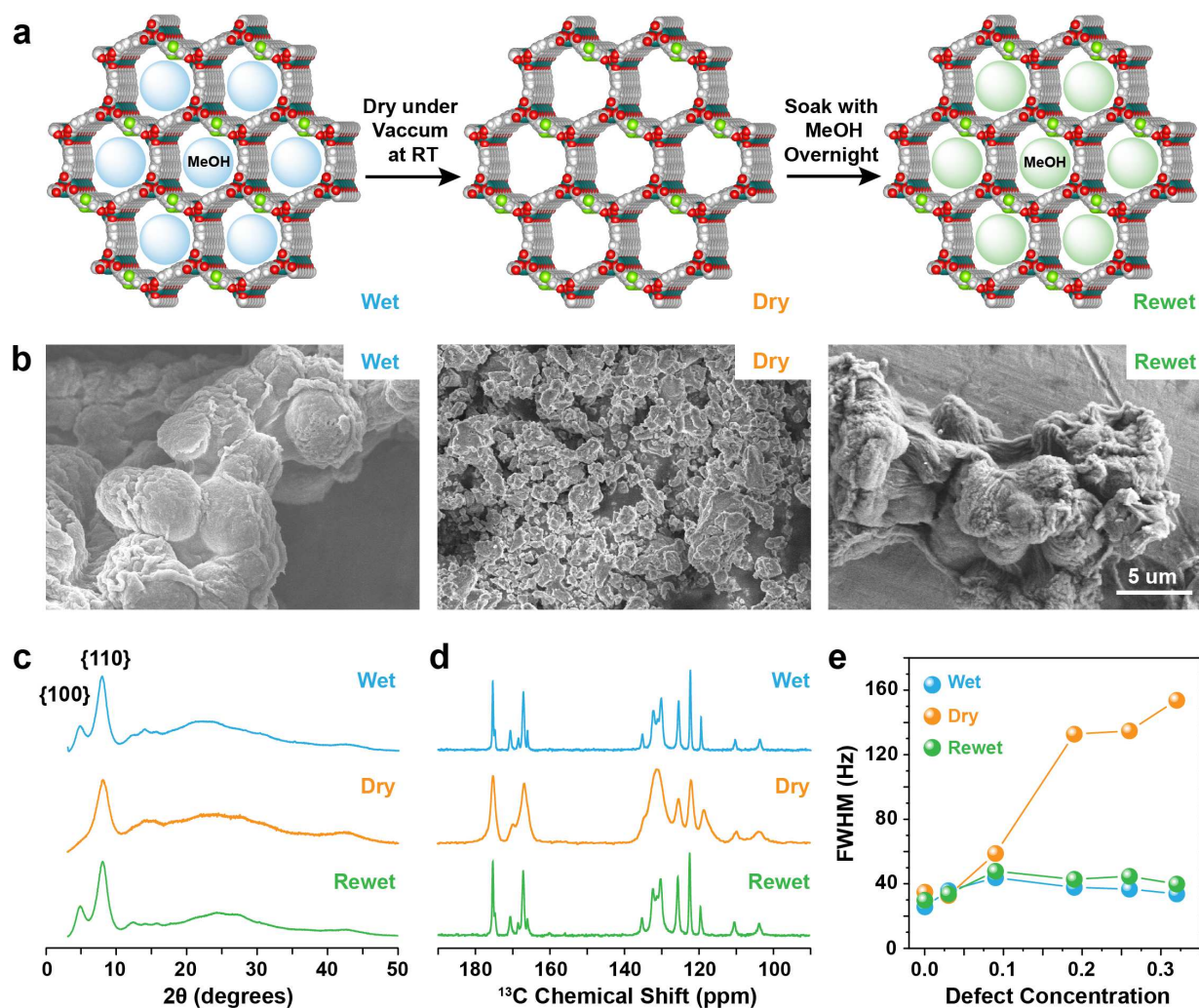**Figure 2. The dynamic structural changes of defective Mg$_2$(dobpdc).** (**a**) Illustrations of solvent (i.e. methanol) removal and re-introduction in Mg$_2$(dobpdc). Characterizations of the "wet", "dry" and "rewet" samples (0.32D): (**b**) SEM images. Scale bar: 5 µm (for all images); (**c**) PXRD patterns, and (**d**) ^{13}C CPMAS spectra of the defective Mg$_2$(dobpdc) under different conditions. (**e**) The FMHW of ^{13}C peak at 122 ppm plotted against the defect concentration. The FMHW can be regarded as the representation of "degree of disorder" for local chemical bonds in the MOF samples.

Still, the PXRD data characterize portions of the lattice with long-range order and provide limited information on disordered portions of the structure for a defective MOF. SSNMR can supplement PXRD to provide a more holistic picture of such partially disordered materials. For instance, the full-width-at-half-maximum (FWHM) of ^{13}C cross-polarization magic-angle spinning (CPMAS) signals (Fig. 2d) shows significant differences between the "dry" and "wet" samples. The FWHM corresponds to the degree of disorder of local chemical bonds, including primarily variations in the bond lengths and torsion angles. Here, the effects of motion-induced T_2 relaxation can be neglected as it only contributes a minor faction of FWHM (Fig. S7). The measurement (Fig. 2e, S7) shows that the "dry" samples generally have a higher degree of disorder than the corresponding "wet" or "rewet" samples (the 122 ppm peak of the dobpdc^{4-} linker is used as representative). The local disorder of the framework gradually increases as more defects are

introduced. Moreover, the degree of order is about the same for both "wet" and "rewet" samples, indicating a reversible order-to-disorder transition. The PXRD and SSNMR characterizations on the series of samples demonstrate that the flexibility of both long-range and local ordering can be tuned continuously by varying the concentration of defects.

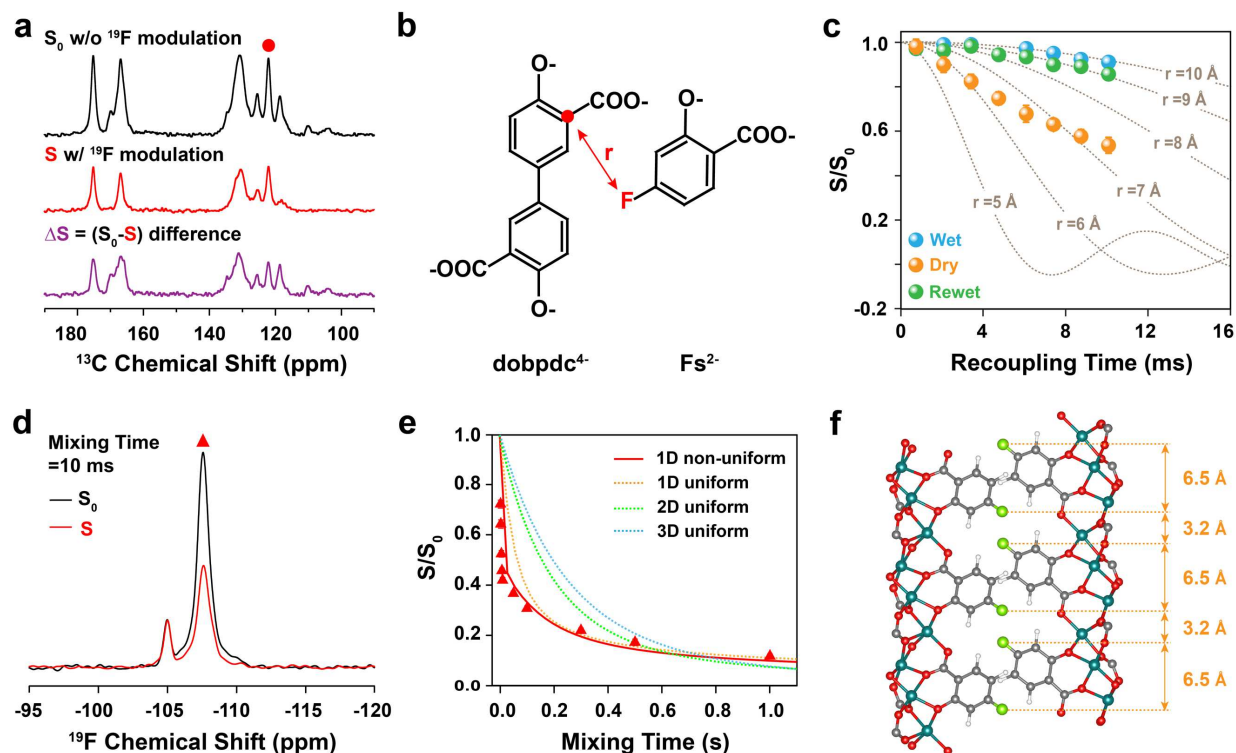## The structure and geometric alignment of defects

Figure 3. Measurements of intermolecular separations. (**a**) Representative ^{13}C spectra obtained in $^{13}C\{^{19}F\}$ REDOR experiments. Spectrum S_0 represents the ^{13}C spectrum taken without ^{19}F dipolar modulation, S is the ^{13}C spectrum with ^{19}F dipolar modulation, and ΔS is the difference spectrum obtained by subtracting S from S_0. (**b**) Schematic illustration of the internuclear distance between the ^{13}C spins (marked as the red dot) on dobpdc^{4-} linker and the ^{19}F spins on the Fs^{2-} ligand measured by the REDOR experiments. (**c**) $^{13}C\{^{19}F\}$ REDOR decay curves for the 0.32D sample measured at 300 K. The dotted lines are theoretical REDOR curves for isolated ^{13}C-^{19}F spin pairs of internuclear distance r. (**d**) Representative ^{19}F reference signal (S_0) and decay signal (S) measured with a ^{19}F CODEX experiment. (**e**) ^{19}F CODEX S/S_0 decay of the -108 ppm peak for the "wet" 0.32D sample measured at 300 K. The solid and dotted lines are simulation results based on different spatial distributions as shown in Fig. S14. (**f**) Structure depicting the directional alignment of Fs^{2-} ligands in parallel with the c axis in defective Mg$_2$(dobpdc). Blue, red, grey, white and green spheres represent Mg, O, C, H and F atoms, respectively.

It is intriguing that Mg$_2$(dobpdc) can accommodate such a high density of defects while maintaining the honeycomb topology. The coordination structure of the Fs^{2-} ligands is important for understanding the defect formation in the framework. Based on the variable contact time ^{13}C CPMAS experiments (Fig. S9) and assisted with $^{13}C\{^{19}F\}$ rotation-echo double-resonance (REDOR) (Fig. S10 and S11), we distinguished the ^{13}C NMR signals that belong to the Fs^{2-} ligand and dobpdc^{4-} linker individually. The assignments of characteristic ^{13}C peaks are shown in Fig.

6

S9. The apparent shift of resonance positions in Fs^{2-} ligand from those in the H_2Fs precursor is consistent with the deprotonation of the carboxylate and hydroxyl groups.

The REDOR experiment is a powerful technique for accurately determining internuclear distances in simple spin systems [39,42]. It measures the spin-spin dipolar interaction (for ^{13}C and ^{19}F here), which correlates with the ^{13}C-^{19}F distance (when the spins are rigid). The experiments render decay curves of relative intensity (S/S_0) of ^{13}C signal under variable periods of ^{19}F irradiation (Fig. 3a, c). The $^{13}C\{^{19}F\}$ REDOR curves that correspond to *intramolecular* ^{13}C-^{19}F interactions between Fs^{2-} linkers (Fig. S11) agree with the expected intramolecular distances analytically. The agreeable results and multiple variable-temperature experiments (Fig. S12) indicate that motional interference is absent on the time-scale of our NMR measurements.

We further investigated the *intermolecular* ^{13}C-^{19}F interactions for ^{13}C spins on dobpdc^{4-} linkers and ^{19}F spins on Fs^{2-} ligands. Due to the heterogeneous spatial arrangements of linkers and defects in defective $Mg_2(dobpdc)$, the intermolecular ^{13}C-^{19}F interaction reflects the highly complex multi-spin system. For a simplified treatment, we can derive the average distances between dobpdc^{4-} and Fs^{2-} at the specified positions (indicated in red in Fig. 3b). We find that the average intermolecular separation decreases to ~6-7 Å in the "dry" 0.32D sample as compared to ~10 Å in the "wet" or ~9 Å in the "rewet" sample (Fig. 3c). This decrease is likely due to the shrinkage of pore volume in the "dry" sample. The almost-complete restoration of intermolecular distance in the "rewet" sample also supports the reversible transition, as described in the previous section. Consistent results are observed for other ^{13}C-^{19}F spin pairs and in the sample with a lower density of defects (Fig. S12).

To further understand the spatial arrangement of the Fs^{2-} ligands, we took advantage of the *intermolecular* ^{19}F-^{19}F spin-spin interactions that are contributed to by fluorine atoms on the Fs^{2-} ligands. The ^{19}F-^{19}F interaction can be probed by a ^{19}F centerband-only detection of exchange (CODEX) experiment, which examines the propagation of through-space spin diffusion process (involving both ^{19}F and ^1H spins) [43,44]. Notably, the dominant ^{19}F signal at -108 ppm (92% molar fraction) of the "wet" 0.32D sample was affected by the CODEX measurement while the minor signal at -105 ppm (8% molar fraction) was not, suggesting only a minor proportion of the Fs^{2-} ligands are isolated and have no Fs^{2-} neighbors (Fig. 3d, S13).

CODEX measurements provide a relative intensity (S/S_0) of the ^{19}F signal under variable mixing periods of spin diffusion (Fig. 3e). The curves not only correlate to the ^{19}F-^{19}F separations but also can be modeled to infer the spatial distribution of a collection of spins[40]. In the defective $Mg_2(dobpdc)$, we considered four possible geometries of spatial arrangements of Fs^{2-} ligands: three-dimensional (3D), two-dimensional (2D), and one-dimensional arrangements with a uniform spacing (1D uniform) and with non-uniform spacings (1D non-uniform), as illustrated in Fig. S14. The numerical model[43] shows that the experimental ^{19}F CODEX curve is best matched by the 1D non-uniform geometry and is incompatible with other geometries (Fig. 3e, S15). This result is consistent with the model of defective $Mg_2(dobpdc)$ optimized by MD simulations in which the Fs^{2-} ligands are aligned along the c-axis of the lattice and the separations between ^{19}F spins are 3.2 and 6.5 Å (Fig. 3f). The alignment of Fs^{2-} ligands in defective $Mg_2(dobpdc)$ is also evidenced in samples with various defect concentrations, or in samples prepared under different treatment conditions (wet, dry, or rewet) (Fig. S16, S17). Nevertheless, the ^{19}F CODEX experiment alone cannot offer accurate determination of intermolecular distances, because the CODEX decay also depends on the proton spin diffusion efficiency[43] which could be largely affected by the density and mobility of solvent molecules. Additional analyses are needed to decipher the topological arrangement of defects as well as their structural transitions.

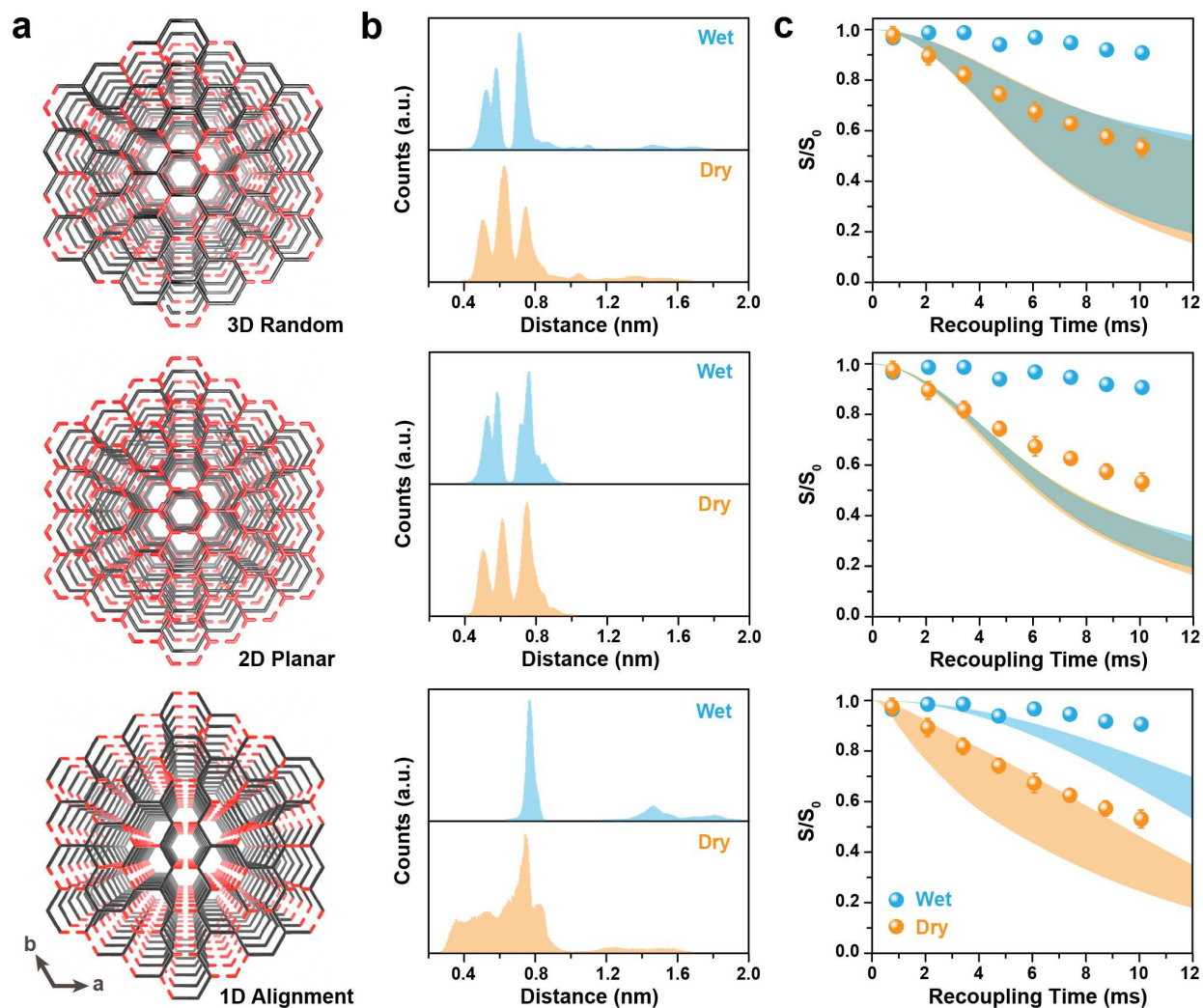**The topological distribution of defects**

Figure 4. Determining the topological distribution of defects. (**a**) The hypothetical defect distributions in defective Mg$_2$(dobpdc): (top) 3D random distribution, (middle) 2D planar distribution in layers, and (bottom) 1D alignment in parallel with the *c*-axis. The Fs^{2-} ligands are shown as dashed red lines and dobpdc^{4-} linkers are shown as black lines. (**b**) The statistical distribution of distances between the selected carbon atoms of dobpdc^{4-} (at 122 ppm) and the nearest F atoms of Fs^{2-}. The results were obtained from the corresponding structural motifs that were optimized by MD simulations for both "wet" and "dry" conditions. (**c**) The calculated ^{13}C{^{19}F} REDOR curves based on the ^{13}C-^{19}F distance distributions for different scenarios. As each scenario corresponds to a number of possible motifs, the REDOR curves are shown as colored bands (blue for "wet" and orange for "dry") to show the spread of ranges. Experimental REDOR data points are shown as colored spheres.

^{13}C{^{19}F} REDOR measurements have the high sensitivity and accuracy to quantify ^{13}C-^{19}F distances and the results can be used as a quantitative determinant of spatial arrangement[39]. Therefore, we attempted to further validate the proposed 1D alignment of defects using ^{13}C{^{19}F} REDOR experiments. To do this, we constructed a library of comprehensive defect models (Scheme S3), all of which were refined by MD simulations, and then analyzed against features of

8

the calculated REDOR curves. The hypothetical models take the known concentration of Fs^{2-} ligands (i.e. $n(Fs^{2-})$:$n(dobpdc^{4-}) = \sim1{:}1$ in the 0.32D sample) and consider the possible distributions in an extended super lattice. The initial models are filled with methanol solvent to represent the "wet" state.

In general, these models can be categorized into three scenarios: a completely random distribution of defects in the 3D lattice (Fig. 4a, top), 2D extended defects in the *ab* plane interlayered randomly between non-defect planes (Fig. 4a, middle), and 1D stacked defects aligned along the *c*-axis (Fig. 4a, bottom). Based on these scenarios, the distributions of intermolecular ^{13}C-^{19}F distances considering the nearest neighbors of $dobpdc^{4-}$ linkers and Fs^{2-} ligands can be obtained (Fig. 4b). The hypothetical $^{13}C\{^{19}F\}$ REDOR curves corresponding to the ^{13}C-^{19}F distance distributions are plotted in Fig. 4c. Because a number of possible models have been analyzed, the REDOR curves are shown collectively as spread bands instead of as individual lines. The spread of REDOR curves for the 3D random distribution is relatively broad because there are a greater number of possibilities, while the spread for the 2D planar and 1D aligned distributions is relatively narrow.

In a further crucial step, we consider the order-to-disorder transition from the "wet" state to the "dry" state. The "dry" models were obtained through MD optimizations of the structures without physically adsorbed methanol. As we expected, the local coordination structure for the Fs^{2-} ligands becomes more disordered in the "dry" state (as shown in the schematic illustrations in Fig. S18-S21). However, the most significant feature appeared in the 1D aligned scenario in which the honeycomb topology is drastically distorted (Fig. S20 and S21), and this led to an obvious difference in the ^{13}C-^{19}F distance distribution (Fig. 4b). In contrast, the lattices for the 3D random and 2D planar scenarios were not significantly affected by solvent removal (Fig. S18-19).
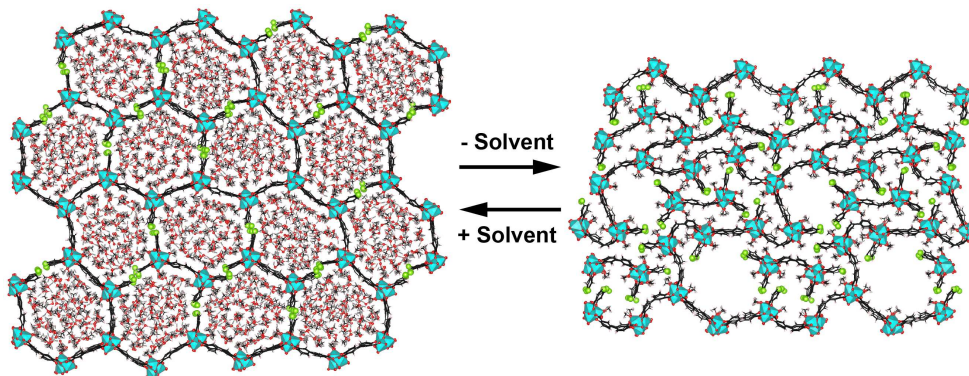

Figure 5. The order-to-disorder transition for defective Mg₂(dobpdc) with 1D aligned defects. The order-to-disorder transition is induced by methanol removal or re-introduction. Blue polyhedra represent MgO_6 units. Red, black and green spheres represent O, C and F atoms, respectively.

By comparing the REDOR curves of both the "wet" and "dry" states between hypothetical models and the experimental data (Fig. 4c), we conclude that a 1D aligned distribution is the most probable scenario for defective Mg₂(dobpdc). This alignment of the Fs^{2-} ligands is also supported by density functional theory (DFT) calculations which show that aligned Fs^{2-} ligands along c-axis are more energetically stable than neighboring arrangement in the *ab* plane (Fig. S22). The deviations of the experimental REDOR curves from the 1D aligned models (Fig. 4c, bottom) at the longer mixing times could arise from the small fraction of isolated Fs^{2-} ligands.

9

The proposed superlattice for defective Mg_2(dobpdc) with 1D aligned defects and a representative structure upon its reversible order-to-disorder transition are illustrated in Fig. 5. These structures were obtained from MD simulations. The shrinkage of the framework after solvent removal is consistent with the $^{13}C\{^{19}F\}$ REDOR results. The preservation of the coordination and bond angles between Mg^{2+} and the dobpdc^{4+} linkers in the "dry" state can account for the remaining {110} PXRD peak (Fig. 2c). The lattice distortion in the dry sample is largely due to the mismatch between Fs^{2-} ligands, which creates disordered regions in the structure. The alignment of defects is crucial for the reversible topological deformation owing to the collective structural changes in the non-bonding linkages.

Conclusion

In summary, we have successfully engineered a flexible MOF matrix by introducing tunable ratios of defects. Our study not only uncovers the unusual 1D alignment of defects, but also offers an understanding of the order-to-disorder transitions in a partially disordered framework. The combined SSNMR strategy for unveiling linker defect distributions is indispensable for studying complex hybrid structures with or without long range ordering.

Author contributions: Conceptualization: YF, XK, JAR, AF, JRL; Sample preparations: YF; Characterizations: YF, WC, JY, LG, QC; Analysis: YF, XK, AF, JAR, MC; Simulations: ZK, ZP, TH, YF, QW; Writing: YF, XK, AF, JAR, JRL.

Competing interests: Authors declare that they have no competing interests.

Data and materials availability: All data are available in the main text or the supplementary materials.

References

1. Krause, S. *et al.* A pressure-amplifying framework material with negative gas adsorption transitions. *Nature* **532**, 348–352 (2016).

2. Pallach, R. *et al.* Frustrated flexibility in metal-organic frameworks. *Nat. Commun.* **12**, 1–12 (2021).

3. Warren, J. E. *et al.* Shape Selectivity by Guest-Driven Restructuring of a Porous Material. *Angew. Chem. Int. Ed.* **126**, 4680–4684 (2014).

4. Matsuda, R. Selectivity from flexibility. *Nature* **509**, 434–435 (2014).

5. Eddaoudi, M. *et al.* Systematic design of pore size and functionality in isoreticular MOFs and their application in methane storage. *Science* **295**, 469–472 (2002).

6. Zhou, H. C. J. & Kitagawa, S. Metal-Organic Frameworks (MOFs). *Chem. Soc. Rev.* **43**, 5415–5418 (2014).

7. Schneemann, A. *et al.* Flexible metal-organic frameworks. *Chem. Soc. Rev.* **43**, 6062–6096 (2014).

8. Vukotic, V. N., Harris, K. J., Zhu, K., Schurko, R. W. & Loeb, S. J. Metal-organic frameworks

with dynamic interlocked components. *Nat. Chem.* **4**, 456–460 (2012).

9. Loiseau, T. *et al.* A Rationale for the Large Breathing of the Porous Aluminum Terephthalate (MIL-53) Upon Hydration. *Chem. - A Eur. J.* **10**, 1373–1382 (2004).

10. Mellot-Draznieks, C., Serre, C., Surblé, S., Audebrand, N. & Férey, G. Very large swelling in hybrid frameworks: A combined computational and powder diffraction study. *J. Am. Chem. Soc.* **127**, 16273–16278 (2005).

11. Meng, W. *et al.* An elastic metal–organic crystal with a densely catenated backbone. *Nature* **598**, 298–303 (2021).

12. Bennett, T. D., Cheetham, A. K., Fuchs, A. H. & Coudert, F. X. Interplay between defects, disorder and flexibility in metal-organic frameworks. *Nat. Chem.* **9**, 11–16 (2016).

13. Cairns, A. B. & Goodwin, A. L. Structural disorder in molecular framework materials. *Chem. Soc. Rev.* **42**, 4881–4893 (2013).

14. Bennett, T. D. & Cheetham, A. K. Amorphous metal-organic frameworks. *Acc. Chem. Res.* **47**, 1555–1562 (2014).

15. Ehrling, S. *et al.* Adaptive response of a metal–organic framework through reversible disorder–disorder transitions. *Nat. Chem.* **13**, 568–574 (2021).

16. Bueken, B. *et al.* A Breathing Zirconium Metal-Organic Framework with Reversible Loss of Crystallinity by Correlated Nanodomain Formation. *Chem. - A Eur. J.* **22**, 3264–3267 (2016).

17. Fu, Y. *et al.* Duet of Acetate and Water at the Defects of Metal–Organic Frameworks. *Nano Lett.* **19**, 1618–1624 (2019).

18. Tan, K. *et al.* Defect Termination in the UiO-66 Family of Metal-Organic Frameworks: The Role of Water and Modulator. *J. Am. Chem. Soc.* **143**, 6328–6332 (2021).

19. McDonald, T. M. *et al.* Cooperative insertion of CO_2 in diamine-appended metal-organic frameworks. *Nature* **519**, 303–308 (2015).

20. Kim, E. J. *et al.* Cooperative carbon capture and steam regeneration with tetraamine-appended metal-organic frameworks. *Science* **369**, 392–396 (2020).

21. Forse, A. C. *et al.* Unexpected Diffusion Anisotropy of Carbon Dioxide in the Metal-Organic Framework $Zn_2(dobpdc)$. *J. Am. Chem. Soc.* **140**, 1663–1673 (2018).

22. Caskey, S. R., Wong-Foy, A. G. & Matzger, A. J. Dramatic tuning of carbon dioxide uptake via metal substitution in a coordination polymer with cylindrical pores. *J. Am. Chem. Soc.* **130**, 10870–10871 (2008).

23. Britt, D., Furukawa, H., Wang, B., Glover, T. G. & Yaghi, O. M. Highly efficient separation of carbon dioxide by a metal-organic framework replete with open metal sites. *Proc. Natl. Acad. Sci. U. S. A.* **106**, 20637–20640 (2009).

24. Lefton, J. B. *et al.* Defects Formation and Amorphization of Zn-MOF-74 Crystals by Post-Synthetic Interactions with Bidentate Adsorbates. *J. Mater. Chem. A* **74**, (2021).

25. Morales-Vidal, J., García-Muelas, R. & Ortuño, M. A. Defects as catalytic sites for the oxygen evolution reaction in Earth-abundant MOF-74 revealed by DFT. *Catal. Sci. Technol.* **11**, 1443–1450 (2021).

26. Wu, D., Yan, W., Xu, H., Zhang, E. & Li, Q. Defect engineering of Mn-based MOFs with rod-shaped building units by organic linker fragmentation. *Inorganica Chim. Acta* **460**, 93–98 (2017).

27. Li, B. & Zeng, H. C. Synthetic Chemistry and Multifunctionality of an Amorphous Ni-MOF-74 Shell on a Ni/SiO2 Hollow Catalyst for Efficient Tandem Reactions. *Chem. Mater.* **31**, 5320–5330 (2019).

28. Ma, P. *et al.* Heterogeneous Amorphous Cu–MOF-74 Catalyst for C-N Coupling Reaction. *ChemistrySelect* **3**, 10694–10700 (2018).

29. Villajos, J. A., Jagorel, N., Reinsch, S. & Emmerling, F. Increasing Exposed Metal Site Accessibility in a Co-MOF-74 Material With Induced Structure-Defects. *Front. Mater.* **6**, 1–10

(2019).

30. Liu, L. *et al.* Imaging defects and their evolution in a metal–organic framework at sub-unit-cell resolution. *Nat. Chem.* **11**, 622–628 (2019).

31. Cliffe, M. J. *et al.* Correlated defect nanoregions in a metal-organic framework. *Nat. Commun.* **5**, 1–8 (2014).

32. Trickett, C. A. *et al.* Definitive Molecular Level Characterization of Defects in UiO-66 Crystals. *Angew. Chem. Int. Ed.* **54**, 11162–11167 (2015).

33. Fu, Y., Guan, H., Yin, J. & Kong, X. Probing molecular motions in metal-organic frameworks with solid-state NMR. *Coord. Chem. Rev.* **427**, 213563 (2021).

34. Rossini, A. J. *et al.* Dynamic nuclear polarization enhanced solid-state NMR spectroscopy of functionalized metal-organic frameworks. *Angew. Chem. Int. Ed.* **51**, 123–127 (2012).

35. Hong, M. & Schmidt-Rohr, K. Magic-angle-spinning NMR techniques for measuring long-range distances in biological macromolecules. *Acc. Chem. Res.* **46**, 2154–2163 (2013).

36. Schmidt-Rohr, K. & Spiess, H. W. *Multidimensional Solid-State NMR and Polymers. Academic Press: Waltham, MA* (Academic Press: Waltham, MA, 1994).

37. Sutrisno, A. & Huang, Y. Solid-state NMR: A powerful tool for characterization of metal-organic frameworks. *Solid State Nucl. Magn. Reson.* **49**–**50**, 1–11 (2013).

38. Ashbrook, S. E., Dawson, D. M. & Seymour, V. R. Recent developments in solid-state NMR spectroscopy of crystalline microporous materials. *Phys. Chem. Chem. Phys.* **16**, 8223–8242 (2014).

39. Kong, X. *et al.* Mapping of Functional Groups in Metal-Organic Frameworks. *Science* **341**, 882–885 (2013).

40. Pang, Z., Zhang, J., Cao, W., Kong, X. & Peng, X. Partitioning surface ligands on nanocrystals for maximal solubility. *Nat. Commun.* **10**, 1–8 (2019).

41. McDonald, T. M. *et al.* Capture of carbon dioxide from air and flue gas in the alkylamine-appended metal-organic framework mmen-Mg2(dobpdc). *J. Am. Chem. Soc.* **134**, 7056–7065 (2012).

42. Gullion, T. & Schaefer, J. Development of REDOR rotational-echo double-resonance NMR. *J. Magn. Reson.* **81**, 196–200 (1989).

43. Luo, W. & Hong, M. Determination of the Oligomeric Number and Intermolecular Distances of Membrane Protein Assemblies by Anisotropic 1H-Driven Spin Diffusion NMR Spectroscopy. *J. Am. Chem. Soc.* **128**, 7242–7251 (2006).

44. DeAzevedo, E. R., Hu, W.-G., Bonagamba, T. J. & Schmidt-Rohr, K. Centerband-Only Detection of Exchange: Efficient Analysis of Dynamics in Solids by NMR. *J. Am. Chem. Soc.* **121**, 8411–8412 (1999).

Supplementary Files

This is a list of supplementary files associated with this preprint. Click to download.

- FinalSINC.pdf